

## Rod-, flower-, and dumbbell-like MnO<sub>2</sub>: Highly active catalysts for the combustion of toluene

Fengjuan Shi<sup>a</sup>, Fang Wang<sup>a</sup>, Hongxing Dai<sup>a,\*</sup>, Jianxing Dai<sup>b</sup>, Jiguang Deng<sup>a</sup>, Yuxi Liu<sup>a</sup>, Guangmei Bai<sup>a</sup>, Kemeng Ji<sup>a</sup>, Chak Tong Au<sup>c,\*\*</sup>

<sup>a</sup> Laboratory of Catalysis Chemistry and Nanoscience, Department of Chemistry and Chemical Engineering, College of Environmental and Energy Engineering, Beijing University of Technology, Beijing 100124, China

<sup>b</sup> Office 7143, Nanchang Military Academy, Nanchang 330103, Jiangxi Province, China

<sup>c</sup> Department of Chemistry, Hong Kong Baptist University, Kowloon Tong, Hong Kong, China

### ARTICLE INFO

#### Article history:

Received 14 January 2012

Received in revised form 5 April 2012

Accepted 14 May 2012

Available online 22 May 2012

#### Keywords:

Hydrothermal preparation method

Water-bathing preparation method

Well-defined morphology

Manganese oxide catalyst

Toluene combustion

### ABSTRACT

The rod-like tetragonal  $\alpha$ -MnO<sub>2</sub>, flower-like hexagonal  $\varepsilon$ -MnO<sub>2</sub>, and dumbbell-like tetragonal  $\beta$ -MnO<sub>2</sub> were prepared using the hydrothermal or water-bathing method under different conditions. It is shown that the  $\alpha$ -MnO<sub>2</sub>,  $\varepsilon$ -MnO<sub>2</sub>, and  $\beta$ -MnO<sub>2</sub> catalysts possessed a surface area of ca. 53, 30, and 114 m<sup>2</sup>/g, respectively. The oxygen adspecies concentration and low-temperature reducibility decreased in the order of  $\alpha$ -MnO<sub>2</sub> >  $\varepsilon$ -MnO<sub>2</sub> >  $\beta$ -MnO<sub>2</sub>, coinciding with the sequence of their catalytic activities for toluene combustion. The well-defined morphological MnO<sub>2</sub> catalysts performed much better than the bulk counterpart. At a space velocity of 20,000 mL/(g h), the temperature for 90% toluene conversion was 238, 229, and 241 °C over  $\alpha$ -MnO<sub>2</sub>,  $\varepsilon$ -MnO<sub>2</sub>, and  $\beta$ -MnO<sub>2</sub>, respectively. The apparent activation energies of  $\alpha$ -MnO<sub>2</sub>,  $\varepsilon$ -MnO<sub>2</sub>, and  $\beta$ -MnO<sub>2</sub> were in the range of 20–26 kJ/mol. It is concluded that higher oxygen adspecies concentrations and better low-temperature reducibility were responsible for the good catalytic performance of the  $\alpha$ -MnO<sub>2</sub>,  $\varepsilon$ -MnO<sub>2</sub>, and  $\beta$ -MnO<sub>2</sub> materials.

© 2012 Elsevier B.V. All rights reserved.

### 1. Introduction

Most of volatile organic compounds (VOCs) emitted from industrial and transportation activities are pollutants to the atmosphere and human health. Catalytic combustion is an effective pathway to remove the VOCs. The important aspect of such a technology is the availability of high-performance catalysts. Although the precious metal catalysts perform excellently for the total oxidation of VOCs (e.g., toluene) at low temperatures [1,2], the high cost limits their wide applications. Cheap metal oxide (e.g., Co<sub>3</sub>O<sub>4</sub> [3] and MnO<sub>x</sub> [4])-based materials show good catalytic activities for VOCs combustion at high temperatures [5–7]. Therefore, it is highly desired to develop base metal oxide catalysts that exhibit good performance at low temperatures for the removal of VOCs.

Manganese oxides (MnO<sub>x</sub>) are among the most active oxide catalysts in VOC oxidation [8–12]. The crystal structure of MnO<sub>x</sub> has a great influence on its catalytic performance. For example, the  $\gamma$ -MnO<sub>2</sub> phase was reported to be more active than  $\beta$ -MnO<sub>2</sub> or  $\alpha$ -Mn<sub>2</sub>O<sub>3</sub> in the oxidation of ethanol [10–12]. In the

past years, manganese oxides with different crystal structures and morphologies have been prepared using various methods. For example, Torres et al. [13] prepared mesoporous MnO<sub>x</sub> catalysts and observed their good catalytic activities for the total oxidation of formaldehyde. Lamaita et al. [10] pointed out that  $\alpha$ -Mn<sub>2</sub>O<sub>3</sub> and  $\gamma$ -MnO<sub>2</sub> were more active than  $\beta$ -MnO<sub>2</sub> in the catalytic oxidation of ethanol. Santos et al. [14] claimed that  $\alpha$ -Mn<sub>2</sub>O<sub>3</sub> and  $\beta$ -MnO<sub>2</sub> showed good catalytic performance for the total oxidation of ethyl acetate. He and coworkers [15] fabricated porous cellulose-supported MnO<sub>2</sub> nanosheet catalysts, and observed that such morphological MnO<sub>2</sub> materials exhibited good catalytic activities for the oxidative removal of formaldehyde. After investigating flower-like manganese oxide nanospheres for the oxidation of formaldehyde, Zhou et al. [16] found that the  $\alpha$ -MnO<sub>2</sub> outperformed the other crystalline manganese oxides below 120 °C. Working on the preparation and catalysis of Mn<sub>3</sub>O<sub>4</sub>,  $\alpha$ -Mn<sub>2</sub>O<sub>3</sub>, and  $\beta$ -MnO<sub>2</sub> materials for toluene or benzene combustion, Kim et al. [17] concluded that the catalytic activity decreased in the sequence of Mn<sub>3</sub>O<sub>4</sub> >  $\alpha$ -Mn<sub>2</sub>O<sub>3</sub> >  $\beta$ -MnO<sub>2</sub>. To the best of our knowledge, however, there have so far been rare studies on the catalytic application of MnO<sub>2</sub> with different crystal phases and various well-defined morphologies for the combustion of toluene.

By using the ordered mesoporous silica (KIT-6- or SBA-16)-nanocasting approach, our group have prepared a number of

\* Corresponding author. Tel.: +86 10 6739 6118; fax: +86 10 6739 1983.

\*\* Corresponding author. Tel.: +852 3411 7067; fax: +852 3411 7348.

E-mail addresses: [hxdai@bjut.edu.cn](mailto:hxdai@bjut.edu.cn) (H. Dai), [pctau@hkbu.edu.hk](mailto:pctau@hkbu.edu.hk) (C.T. Au).

mesoporous transition-metal oxides (e.g., chromia [18,19], iron oxide [20], manganese oxide [21], and cobalt oxide [21,22]), and investigated their catalytic properties for the removal of formaldehyde, acetone, methanol, and toluene. Recently, we adopted the hydrothermal or water-bathing strategy to generate numerous transition-metal oxides with well-defined morphologies. In this paper, we report the preparation and catalytic performance of  $\alpha$ -,  $\epsilon$ - or  $\beta$ - $\text{MnO}_2$  with a rod-, flower- or dumbbell-like morphology for the combustion of toluene.

## 2. Experimental

### 2.1. Catalyst preparation

The  $\alpha$ - $\text{MnO}_2$ ,  $\epsilon$ - $\text{MnO}_2$ , and  $\beta$ - $\text{MnO}_2$  catalysts with various morphologies were prepared using the hydrothermal or water-bathing method. The detailed procedures are as follows:

- (i) 8 mmol of  $\text{KMnO}_4$  and 3 mmol of  $\text{MnSO}_4 \cdot \text{H}_2\text{O}$  were dissolved in 80 mL of deionized water, after stirring for 1 h the mixed solution was transferred to a 100-mL autoclave for thermal treatment at  $160^\circ\text{C}$  for 12 h [23];
- (ii) 2 mmol of  $\text{KMnO}_4$  was dissolved in 40 mL of deionized water, and 2 mL of 98 wt.%  $\text{H}_2\text{SO}_4$  solution was dropwise added to the  $\text{KMnO}_4$  solution under stirring, and then a piece of copper plate (2 cm  $\times$  8 cm in dimension) was added to the mixed solution, which was water-bathed at  $60^\circ\text{C}$  for 8 h [24];
- (iii) 4 mmol of  $\text{KMnO}_4$  was dissolved in 80 mL of deionized water under stirring, and 16 mmol of glucose, 1 mL of ethylenediamine (EDA), and 1.4 mL of 37 wt.% HCl solution were added to the  $\text{KMnO}_4$  solution, which was then transferred to a 100-mL autoclave for thermal treatment at  $120^\circ\text{C}$  for 12 h [25].

After being filtered, washed with deionized water three times and absolute ethanol two times, and dried at  $60^\circ\text{C}$  for 24 h, the sample precursor derived from (i), (ii) or (iii) was calcined in a muffle furnace at a ramp of  $1^\circ\text{C}/\text{min}$  from RT to  $300$ ,  $300$  or  $350^\circ\text{C}$  and kept at this temperature for 4 h, thus obtaining the rod-, flower-, and dumbbell-like  $\text{MnO}_2$  catalysts with different crystal phases, respectively.

The bulk  $\text{MnO}_2$  sample (denoted as bulk- $\text{MnO}_2$ ) with a surface area of  $10.1 \text{ m}^2/\text{g}$  and the other chemicals (A.R. in purity) were purchased from Beijing Chemical Company and used without further purification.

### 2.2. Catalyst characterization

Powdered X-ray diffraction (XRD) patterns of the samples were recorded on a Bruker/AXS D8 Advance diffractometer operated at 35 kV and 35 mA using  $\text{Cu K}\alpha$  radiation and a Ni filter ( $\lambda = 0.15406 \text{ nm}$ ). Crystal phases were identified by referring the diffraction lines to those of the powder diffraction files, 1998 ICDD PDF database. The Brunauer–Emmett–Teller (BET) surface areas of the samples were measured via  $\text{N}_2$  adsorption at  $-196^\circ\text{C}$  on an ASAP 2020 adsorption analyzer (Micromeritics) with the samples being outgassed at  $250^\circ\text{C}$  for 2 h under vacuum prior to measurements. The scanning electron microscopic (SEM) images of the samples were recorded on a Gemini Zeiss Supra 55 apparatus operating at 10 kV. By means of a JEOL-2010 instrument (operated at 200 kV), transmission electron microscopic (TEM) and high-resolution TEM images as well as the selected-area electron diffraction (SAED) patterns of the samples were obtained. X-ray photoelectron spectroscopy (XPS, VG CLAM 4 MCD analyzer) was employed to determine the Mn 2p, O 1s, and C 1s binding energies (BEs) of surface species of the as-prepared samples; Mg  $\text{K}\alpha$

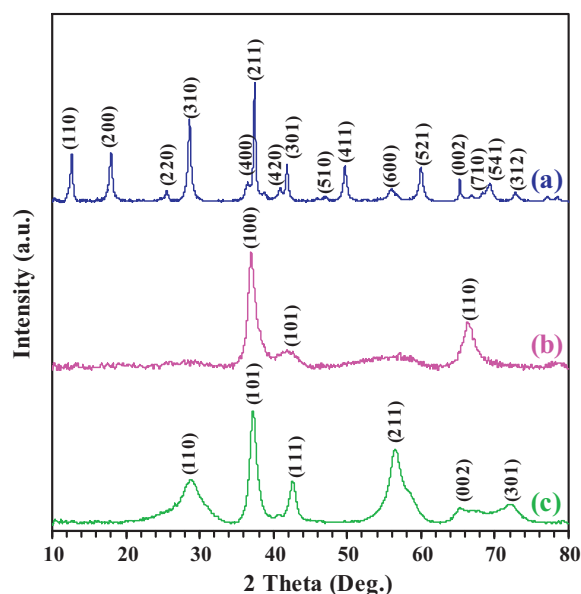


Fig. 1. Wide-angle XRD patterns of (a) rod-like  $\alpha$ - $\text{MnO}_2$ , (b) flower-like  $\epsilon$ - $\text{MnO}_2$ , and (c) dumbbell-like  $\beta$ - $\text{MnO}_2$ .

( $h\nu = 1253.6 \text{ eV}$ ) was used as excitation source and the instrumental resolution was  $0.5 \text{ eV}$ . After treatment in  $\text{O}_2$  (flow rate =  $20 \text{ mL}/\text{min}$ ) at  $500^\circ\text{C}$  for 1 h (for removal of adsorbed water and surface carbonate), the samples were cooled to RT and transferred into the spectrometer under helium (GLOVE BAG, Instruments for Research and Industry, USA). The samples were then degassed in the preparation chamber ( $10^{-5} \text{ Torr}$ ) for 0.5 h and introduced into the analysis chamber ( $3 \times 10^{-9} \text{ Torr}$ ) for spectrum recording. The C 1s signal at  $\text{BE} = 284.6 \text{ eV}$  was taken as reference for BE calibration.

Hydrogen temperature-programmed reduction ( $\text{H}_2$ -TPR) was carried out in the  $50$ – $600^\circ\text{C}$  range on a Micromeritics AutoChem II 2920 apparatus.  $0.1 \text{ g}$  of the sample (40–60 mesh) was treated in a helium flow of  $25 \text{ mL}/\text{min}$  at  $350^\circ\text{C}$  for 1 h and then cooled in the same atmosphere to  $50^\circ\text{C}$ . The sample was then reduced in a flow of  $5\% \text{ H}_2$ – $95\% \text{ Ar}$  (v/v) at a ramp of  $10^\circ\text{C}/\text{min}$ . The outlet gases were analyzed on-line using a thermal conductivity detector (TCD). The TCD responses were calibrated against that of the complete reduction of a known standard CuO sample (Aldrich, 99.995%).

### 2.3. Catalytic evaluation

The catalytic activity was evaluated with the sample charged in a continuous flow fixed-bed quartz microreactor (i.d. =  $4 \text{ mm}$ ). To minimize the effect of hot spots, the catalyst ( $0.1 \text{ g}$ , 40–60 mesh) was diluted with  $0.3 \text{ g}$  of quartz sands (40–60 mesh). The reactant feed (flow rate =  $33.3 \text{ mL}/\text{min}$ ) was  $1000 \text{ ppm}$  toluene +  $\text{O}_2$  +  $\text{N}_2$  (balance) with a toluene/ $\text{O}_2$  molar ratio of  $1/400$ . The space velocity (SV) was  $20,000 \text{ mL}/(\text{g h})$ . The outlet gases were analyzed online by a gas chromatograph (GC-2010, Shimadzu) equipped with a flame ionization detector and a TCD, using a Chromosorb 101 column for toluene and a Carboxen 1000 column for permanent gas separation. The balance of carbon throughout the investigation was estimated to be 99.5%.

## 3. Results and discussion

### 3.1. Crystal structure

Fig. 1 shows the XRD patterns of the as-prepared  $\text{MnO}_2$  catalysts. By referring to the XRD patterns of the standard  $\alpha$ - $\text{MnO}_2$  (JCPDS PDF# 44-0141),  $\epsilon$ - $\text{MnO}_2$  (JCPDS PDF# 30-0820), and  $\beta$ - $\text{MnO}_2$

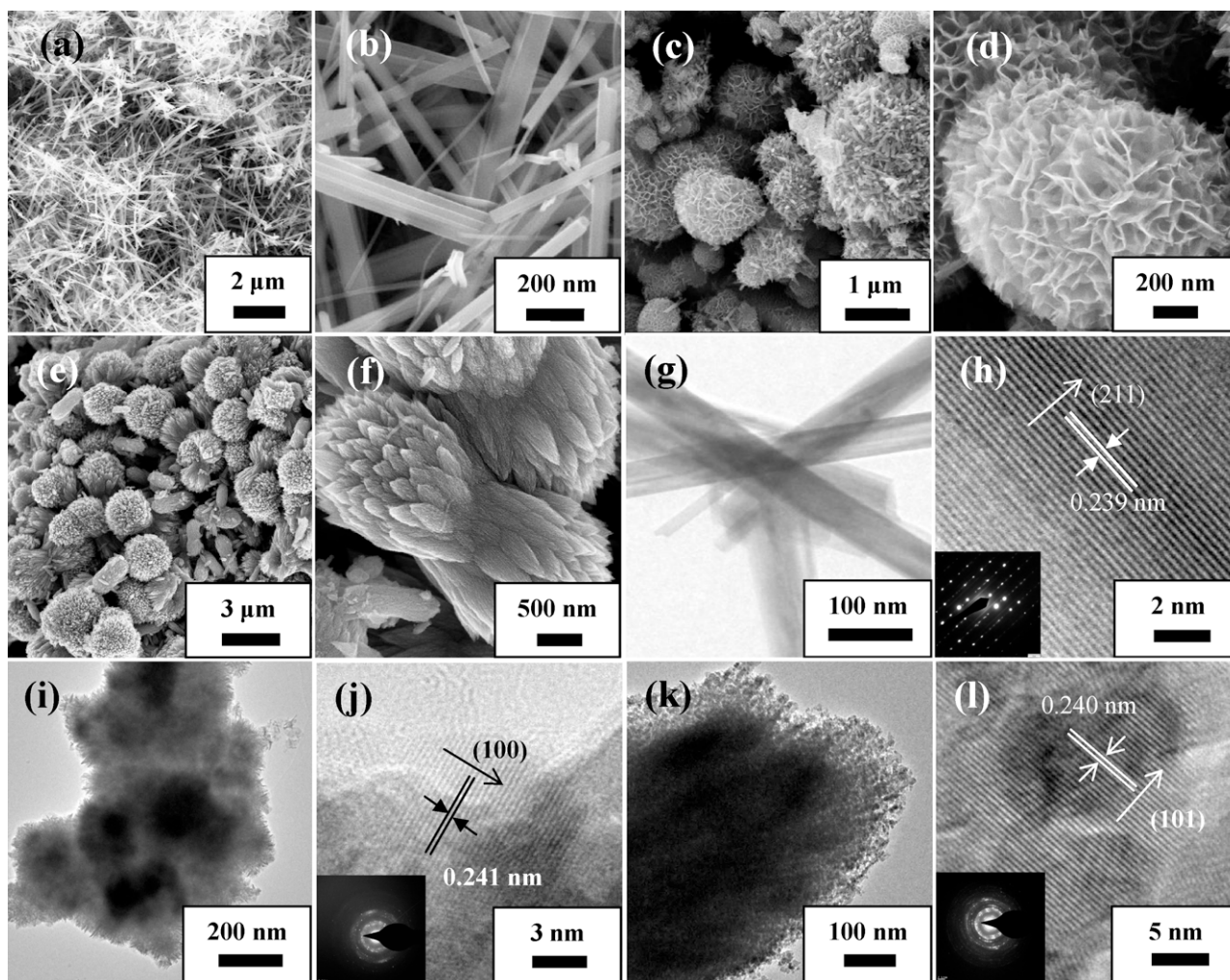


**Fig. 2.** (a–f) SEM and (g–l) TEM images as well as the SAED patterns (insets) of (a, b, g and h) rod-like  $\alpha$ - $\text{MnO}_2$ , (c, d, i and j) flower-like  $\epsilon$ - $\text{MnO}_2$ , and (e, f, k and l) dumbbell-like  $\beta$ - $\text{MnO}_2$ .

(JCPDS PDF# 24-0735), one can deduce that the rod-, flower-, and dumbbell-like manganese oxide samples were single-phase and of tetragonal  $\alpha$ - $\text{MnO}_2$ , hexagonal  $\epsilon$ - $\text{MnO}_2$ , and tetragonal  $\beta$ - $\text{MnO}_2$  crystal structures, respectively. All of the diffraction peaks could be well indexed, as indicated in Fig. 1(a)–(c). The discrepancies in intensity and width of XRD peaks suggest the difference in crystallinity of these samples, with the  $\alpha$ - $\text{MnO}_2$  sample being better than the  $\epsilon$ - and  $\beta$ - $\text{MnO}_2$  samples in crystallinity. Therefore, the XRD results reveal that the crystal structure and crystallinity of the manganese oxide sample were strongly dependent on the preparation method and condition.

### 3.2. Morphology and textural property

Fig. 2 shows the SEM and TEM images as well as the SAED patterns of the as-prepared manganese oxide samples. As can be clearly seen from Fig. 2(a)–(f), the  $\alpha$ - $\text{MnO}_2$  sample derived hydrothermally with  $\text{KMnO}_4$  and  $\text{MnSO}_4 \cdot \text{H}_2\text{O}$  as metal source displayed a rod-like morphology (Fig. 2(a) and (b)), the diameter and length of the rods were mostly ca. 80 nm and 3–6  $\mu\text{m}$ , respectively. The  $\epsilon$ - $\text{MnO}_2$  sample derived from the water-bathing process with  $\text{KMnO}_4$  and copper plate as metal source was flower-like in morphology, which was aggregated by a number of nanoplates (Fig. 2(c) and (d)), the diameter of the flower-like sphere was typically ca. 1.5  $\mu\text{m}$ . In the  $\beta$ - $\text{MnO}_2$  sample fabricated hydrothermally

with  $\text{KMnO}_4$  as Mn source in the presence of glucose, ethylenediamine, and HCl, most of the particles showed a dumbbell-like shape with the ends being flower-like (Fig. 2(e) and (f)), and the dumbbell was roughly 2–4  $\mu\text{m}$  in diameter. From Fig. 2(g)–(l), one can clearly see that the  $\alpha$ - $\text{MnO}_2$  and  $\epsilon$ - $\text{MnO}_2$  samples were nanorod-like and nanoflower-like spherical in morphology (Fig. 2(g) and (i)), respectively, whereas the dumbbell ends of the  $\beta$ - $\text{MnO}_2$  sample were composed of a large number of aggregated nanoparticles (Fig. 3(k)). It is observed from Fig. 3(h), (j), and (l) that there were a large number of well-resolved lattice fringes. The lattice spacings ( $d$  values) of the (2 1 1), (1 0 0), and (1 0 1) crystal planes of the rod-like  $\alpha$ - $\text{MnO}_2$ , flower-like  $\epsilon$ - $\text{MnO}_2$ , and dumbbell-like  $\beta$ - $\text{MnO}_2$  samples were respectively 0.239, 0.241, and 0.240 nm, rather close to the corresponding  $d$  values (0.23950, 0.24200, and 0.24070 nm) of the standard  $\alpha$ - $\text{MnO}_2$  (JCPDS PDF# 44-0141),  $\epsilon$ - $\text{MnO}_2$  (JCPDS PDF# 30-0820), and  $\beta$ - $\text{MnO}_2$  (JCPDS PDF# 24-0735) samples. Furthermore, the recording of linearly aligned bright electron diffraction spots in the SAED pattern (inset of Fig. 3(b)) suggests that the rod-like  $\alpha$ - $\text{MnO}_2$  was single-crystalline; in the SAED patterns of the flower-like spherical  $\epsilon$ - $\text{MnO}_2$  and dumbbell-like  $\beta$ - $\text{MnO}_2$  samples, the appearance of multiple bright electron diffraction rings indicates the formation of polycrystalline  $\epsilon$ - $\text{MnO}_2$  and  $\beta$ - $\text{MnO}_2$ .

As can be seen from Table 1, the crystallite sizes of the rod-like  $\alpha$ - $\text{MnO}_2$ , flower-like  $\epsilon$ - $\text{MnO}_2$ , and dumbbell-like  $\beta$ - $\text{MnO}_2$  samples were 23.1, 5.8, and 6.0 nm, respectively. The BET surface area

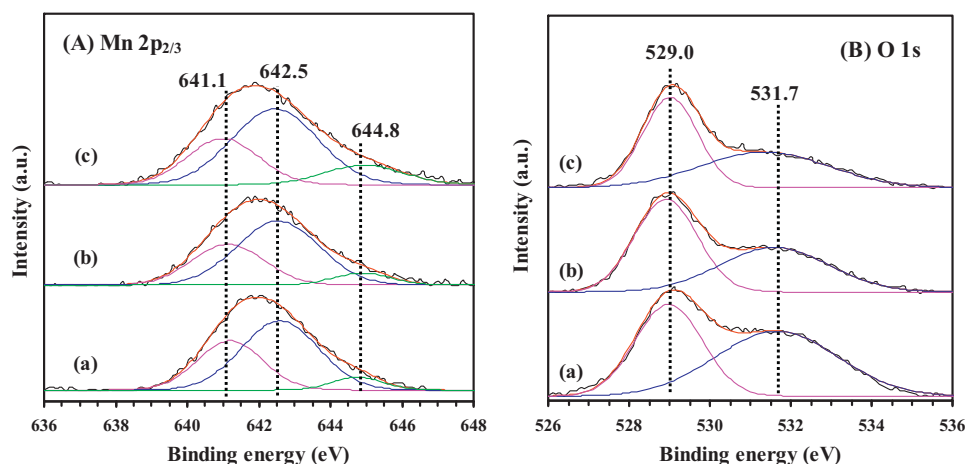


**Fig. 3.** (A) Mn 2p<sub>3/2</sub> and (B) O 1s XPS spectra of (a) rod-like  $\alpha$ -MnO<sub>2</sub>, (b) flower-like  $\epsilon$ -MnO<sub>2</sub>, and (c) dumbbell-like  $\beta$ -MnO<sub>2</sub>.

of the rod-like  $\alpha$ -MnO<sub>2</sub> sample was 53.1 m<sup>2</sup>/g, higher than that (30.3 m<sup>2</sup>/g) of the flower-like  $\epsilon$ -MnO<sub>2</sub> sample. The dumbbell-like  $\beta$ -MnO<sub>2</sub> sample, however, showed a BET surface area of 113.5 m<sup>2</sup>/g, markedly higher than those (30.3–53.1 m<sup>2</sup>/g) of the rod-like  $\alpha$ -MnO<sub>2</sub> and flower-like  $\epsilon$ -MnO<sub>2</sub> samples.

### 3.3. Surface species and reducibility

Fig. 3 illustrates the Mn 2p<sub>3/2</sub> and O 1s XPS spectra of the manganese oxide samples. It is observed from Fig. 3(A) that the asymmetrical Mn 2p<sub>3/2</sub> XPS signal at BE = ca. 642 eV could be decomposed into three components at BE = 641.1, 642.5, and 644.8 eV, assignable to the surface Mn<sup>3+</sup> and Mn<sup>4+</sup> species and the satellite [17,26–28], respectively. A quantitative analysis on the Mn 2p<sub>3/2</sub> XPS spectra of the samples gives rise to the surface Mn<sup>3+</sup>/Mn<sup>4+</sup> molar ratios, as summarized in Table 1. It is clear that the preparation method had an influence on the surface Mn<sup>3+</sup>/Mn<sup>4+</sup> molar ratio of the product, with the rod-like  $\alpha$ -MnO<sub>2</sub> sample possessing the highest surface Mn<sup>3+</sup>/Mn<sup>4+</sup> molar ratio (0.60) whereas the bulk-MnO<sub>2</sub> sample showing the lowest surface Mn<sup>3+</sup>/Mn<sup>4+</sup> molar ratio (0.34). Usually, oxygen molecules are adsorbed at the oxygen vacancies of an oxide material. Therefore, we believe that the oxygen adspecies locate at the surface oxygen vacancies of MnO<sub>2</sub>. Based on the principle of electroneutrality, we deduce that the surface oxygen vacancy density would be the highest on the rod-like  $\alpha$ -MnO<sub>2</sub> surface but the lowest on the bulk-MnO<sub>2</sub> surface. Such a deduction was substantiated by the results of O 1s XPS investigations. As shown in Fig. 3(B), the asymmetrical O 1s signal could be deconvoluted to two components: one at BE = 529.0 eV

and the other at BE = 531.7 eV, the former was ascribable to the surface lattice oxygen (O<sub>latt</sub>) species, whereas the latter to the surface adsorbed oxygen (O<sub>ads</sub>) species [26–29]. After making quantitative analysis (Table 1), one can see that the surface O<sub>ads</sub>/O<sub>latt</sub> molar ratio decreased in the sequence of rod-like  $\alpha$ -MnO<sub>2</sub> (1.28) > flower-like  $\epsilon$ -MnO<sub>2</sub> (0.96) > dumbbell-like  $\beta$ -MnO<sub>2</sub> (0.91) > bulk-MnO<sub>2</sub> (0.78), coinciding with the order of Mn<sup>3+</sup>/Mn<sup>4+</sup> molar ratio of these samples.

Reducibility is an important factor influencing the catalytic activity of a material. Fig. 4(A) illustrates the H<sub>2</sub>-TPR profiles of the MnO<sub>2</sub> samples. The bulk-MnO<sub>2</sub> sample displayed only one reduction peak centered at ca. 510 °C, corresponding to a H<sub>2</sub> consumption of 6.2 mmol/g (Table 2). For the rod-like  $\alpha$ -MnO<sub>2</sub> sample, there were two reduction peaks centered at 245 and 352 °C, corresponding to a H<sub>2</sub> consumption of 6.0 and 3.1 mmol/g (Table 2), respectively; for the flower-like  $\epsilon$ -MnO<sub>2</sub> sample, two reduction peaks centered at 250 and 311 °C appeared and the corresponding H<sub>2</sub> consumptions were 5.0 and 2.9 mmol/g (Table 2); for the dumbbell-like  $\beta$ -MnO<sub>2</sub> sample, however, only one reduction signal at 296 °C was recorded, and the H<sub>2</sub> consumption was 9.3 mmol/g (Table 2). According to the literature [13,17], the reduction process of MnO<sub>2</sub> could be reasonably divided into two steps: (i) MnO<sub>2</sub> → Mn<sub>3</sub>O<sub>4</sub> and (ii) Mn<sub>3</sub>O<sub>4</sub> → MnO, which corresponds to a H<sub>2</sub> consumption of 7.67 and 3.83 mmol/g (totally 11.50 mmol/g). By comparing the theoretical and experimental H<sub>2</sub> consumption data (Table 2), one can see that 69–81% Mn<sup>4+</sup> and Mn<sup>3+</sup> in rod-like  $\alpha$ -MnO<sub>2</sub>, flower-like  $\epsilon$ -MnO<sub>2</sub>, and dumbbell-like  $\beta$ -MnO<sub>2</sub> were reduced to Mn<sup>2+</sup> below 400 °C, whereas less half of Mn<sup>4+</sup> and Mn<sup>3+</sup> in bulk-MnO<sub>2</sub> was reduced to Mn<sup>2+</sup> below 550 °C. Furthermore, the

**Table 1**

Preparation conditions, crystallite sizes, BET surface areas, and surface element compositions of the as-prepared MnO<sub>2</sub> samples.

Sample	Preparation method	Mn source	Calcination condition	Crystallite size <sup>a</sup> (nm)	BET surface area (m <sup>2</sup> /g)	Surface element molar ratio	
						Mn <sup>3+</sup> /Mn <sup>4+</sup>	O <sub>ads</sub> /O <sub>latt</sub>
Bulk-MnO <sub>2</sub>	–	–	–	–	10.1	0.34	0.78
Rod-like $\alpha$ -MnO <sub>2</sub>	Hydrothermal treatment at 160 °C for 12 h	KMnO <sub>4</sub> and MnSO <sub>4</sub>	300 °C, 4 h	23.1	53.1	0.60	1.28
Flower-like $\epsilon$ -MnO <sub>2</sub>	Water-bathing treatment at 60 °C for 8 h	KMnO <sub>4</sub>	300 °C, 4 h	5.8	30.3	0.56	0.96
Dumbbell-like $\beta$ -MnO <sub>2</sub>	Hydrothermal treatment at 120 °C for 12 h	KMnO <sub>4</sub>	350 °C, 4 h	6.0	113.5	0.50	0.91

<sup>a</sup> The data were obtained according to the Scherrer equation using the FWHM of the (1 0 1) line for rod-like  $\alpha$ -MnO<sub>2</sub>, the (1 0 0) line for flower-like  $\epsilon$ -MnO<sub>2</sub>, and the (2 1 1) line for dumbbell-like  $\beta$ -MnO<sub>2</sub>.

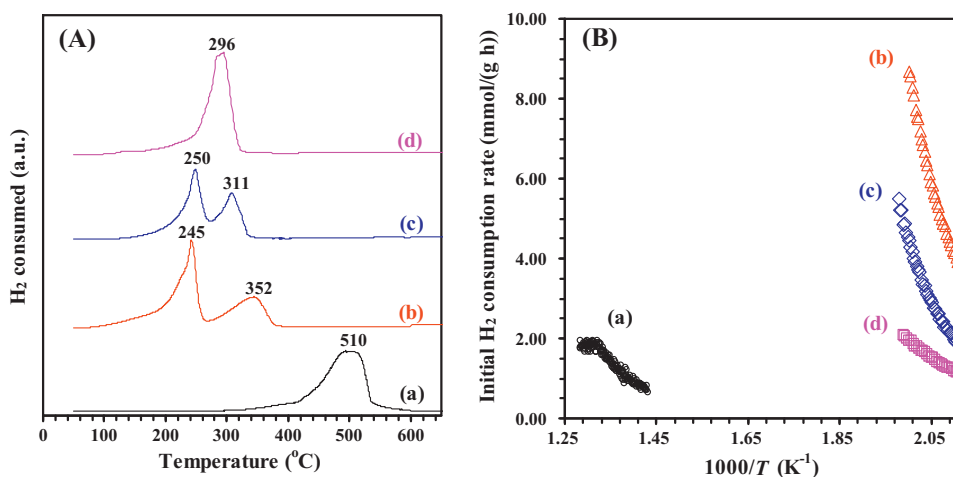


Fig. 4. (A) H<sub>2</sub>-TPR profiles and (B) initial H<sub>2</sub> consumption rates of (a) bulk-MnO<sub>2</sub>, (b) rod-like  $\alpha$ -MnO<sub>2</sub>, (c) flower-like  $\epsilon$ -MnO<sub>2</sub>, and (d) dumbbell-like  $\beta$ -MnO<sub>2</sub>.

first reduction temperatures (245–296 °C) of the rod-like  $\alpha$ -MnO<sub>2</sub>, flower-like  $\epsilon$ -MnO<sub>2</sub>, and dumbbell-like  $\beta$ -MnO<sub>2</sub> samples were much lower than that (510 °C) of the bulk-MnO<sub>2</sub> sample, suggesting that the three well-defined morphological MnO<sub>2</sub> samples were more reducible than the bulk-MnO<sub>2</sub> sample at low temperatures. In other words, the rod-like  $\alpha$ -MnO<sub>2</sub>, flower-like  $\epsilon$ -MnO<sub>2</sub>, and dumbbell-like  $\beta$ -MnO<sub>2</sub> samples exhibited better low-temperature reducibility than the bulk-MnO<sub>2</sub> sample, which was confirmed by the initial H<sub>2</sub> consumption rate of these samples. In order to better compare the low-temperature reducibility of the manganese oxide samples, we calculated the initial H<sub>2</sub> consumption rate of the first reduction peak (where less than 25% oxygen in the sample was removed [30,31]) of each sample, and the results are shown in Fig. 4(B). Obviously, the initial H<sub>2</sub> consumption rate decreased in the order of rod-like  $\alpha$ -MnO<sub>2</sub> > flower-like  $\epsilon$ -MnO<sub>2</sub> > dumbbell-like  $\beta$ -MnO<sub>2</sub> > bulk-MnO<sub>2</sub>. That is to say, the low-temperature reducibility of these samples follow such a sequence, which might be intimately associated with their crystal structures, Mn<sup>3+</sup>/Mn<sup>4+</sup> molar ratios, and morphologies.

### 3.4. Catalytic performance

When only quartz sands were loaded into the microreactor, we detected 10% conversion of toluene at 450 °C (Fig. S1 of the Supplementary material). This result indicates that no homogeneous reactions took place under the adopted reaction conditions (below 400 °C). Fig. 5(A) shows the catalytic performance of the as-prepared MnO<sub>2</sub> and bulk-MnO<sub>2</sub> catalysts for the combustion of toluene. Under the conditions of toluene concentration = 1000 ppm, toluene/O<sub>2</sub> molar ratio = 1/400, and SV = 20,000 mL/(g h), toluene conversion increased monotonously with the rise in reaction temperature; the rod-like  $\alpha$ -MnO<sub>2</sub>, flower-like  $\epsilon$ -MnO<sub>2</sub>, and dumbbell-like  $\beta$ -MnO<sub>2</sub> catalysts showed much better activities than the bulk-MnO<sub>2</sub> catalyst. It is worth pointing out that CO<sub>2</sub> and H<sub>2</sub>O were the only products and the estimated carbon balance was around 99.5%. Therefore, toluene could be completely oxidized

over our catalysts. The reaction temperatures  $T_{50\%}$  and  $T_{90\%}$  (corresponding to the toluene conversion = 50 and 90%) over the MnO<sub>2</sub> catalysts were listed in Table 2. It is observed that the rod-like  $\alpha$ -MnO<sub>2</sub> sample was better at lower temperatures (170–220 °C) than but slightly inferior above 220 °C to the flower-like  $\epsilon$ -MnO<sub>2</sub> sample in catalytic performance; both the rod-like  $\alpha$ -MnO<sub>2</sub> and flower-like  $\epsilon$ -MnO<sub>2</sub> catalysts outperformed the dumbbell-like  $\beta$ -MnO<sub>2</sub> catalyst. Shown in Fig. 5(B) is the effect of SV on the catalytic activity of the rod-like  $\alpha$ -MnO<sub>2</sub> sample. As expected, the toluene conversion increased with the drop in SV at the same reaction temperature, a result due to the prolongation of contact between the reactants and the catalyst. In order to examine the catalytic stability of the rod-like  $\alpha$ -MnO<sub>2</sub> sample, we monitored the toluene conversion at 238 °C within 48 h of on-stream reaction and the result was shown in Fig. 5(C). It is seen that no significant activity losses were detected during the on-stream reaction process. Therefore, the rod-like  $\alpha$ -MnO<sub>2</sub> material was catalytically durable. Furthermore, the H<sub>2</sub>-TPR profile of the used rod-like  $\alpha$ -MnO<sub>2</sub> sample was similar to that of the fresh counterpart (Fig. S2 of the Supplementary material).

The combustion of toluene has been studied over various catalysts in the past years. The rod-like  $\alpha$ -MnO<sub>2</sub>, flower-like  $\epsilon$ -MnO<sub>2</sub>, and dumbbell-like  $\beta$ -MnO<sub>2</sub> samples prepared in the present study showed good catalytic performance ( $T_{50\%}$  = 220–231 °C and  $T_{90\%}$  = 229–241 °C at SV = 20,000 mL/(g h)). Apparently, such catalytic performance was much better than that ( $T_{50\%}$  = 245 °C and  $T_{90\%}$  = 270 °C at SV = 15,000 mL/(g h)) over Mn<sub>3</sub>O<sub>4</sub> [17], that ( $T_{50\%}$  = 280 °C and  $T_{90\%}$  = 295 °C at SV = 15,000 mL/(g h)) over  $\alpha$ -Mn<sub>2</sub>O<sub>3</sub> [17], that ( $T_{50\%}$  = 340 °C and  $T_{90\%}$  = 375 °C at SV = 15,000 mL/(g h)) over  $\beta$ -MnO<sub>2</sub> [17], that ( $T_{50\%}$  = 254 °C and  $T_{90\%}$  = 295 °C at SV = 178 h<sup>-1</sup>) over LaMnO<sub>3</sub> [32], that ( $T_{50\%}$  = 270 °C and  $T_{90\%}$  = 300 °C at SV = 186 h<sup>-1</sup>) over 5 wt.% Au/CeO<sub>2</sub> [33], and that ( $T_{90\%}$  = 250 °C at SV = 18,000 mL/(g h)) over 0.5 wt.% Pd/LaMnO<sub>3</sub> [34].

It is well accepted that the oxidation of organic molecules over the transition metal oxide catalysts involves a Mars–van Krevelen mechanism, where the organic molecule is oxidized by

Table 2  
Reduction temperatures, H<sub>2</sub> consumption, catalytic activities (at SV = 20,000 mL/(g h)), and kinetic parameters of the MnO<sub>2</sub> samples.

Sample	Reduction temperature (°C)		H <sub>2</sub> consumption (mmol/g)			Catalytic activity (°C)		Kinetic parameter		
	Peak 1	Peak 2	Peak 1	Peak 2	Total	$T_{50\%}$	$T_{90\%}$	$A$ (s <sup>-1</sup> )	$E_a$ (kJ/mol)	$R^2$
Bulk-MnO <sub>2</sub>	510	–	6.2	–	6.2	284	317	$8.06 \times 10^6$	74.3	0.982
Rod-like $\alpha$ -MnO <sub>2</sub>	245	352	6.0	3.1	9.1	220	238	29.1	19.6	0.913
Flower-like $\epsilon$ -MnO <sub>2</sub>	250	311	5.0	2.9	7.9	221	229	$1.30 \times 10^2$	26.1	0.957
Dumbbell-like $\beta$ -MnO <sub>2</sub>	296	–	9.3	–	9.3	231	241	58.0	23.6	0.956

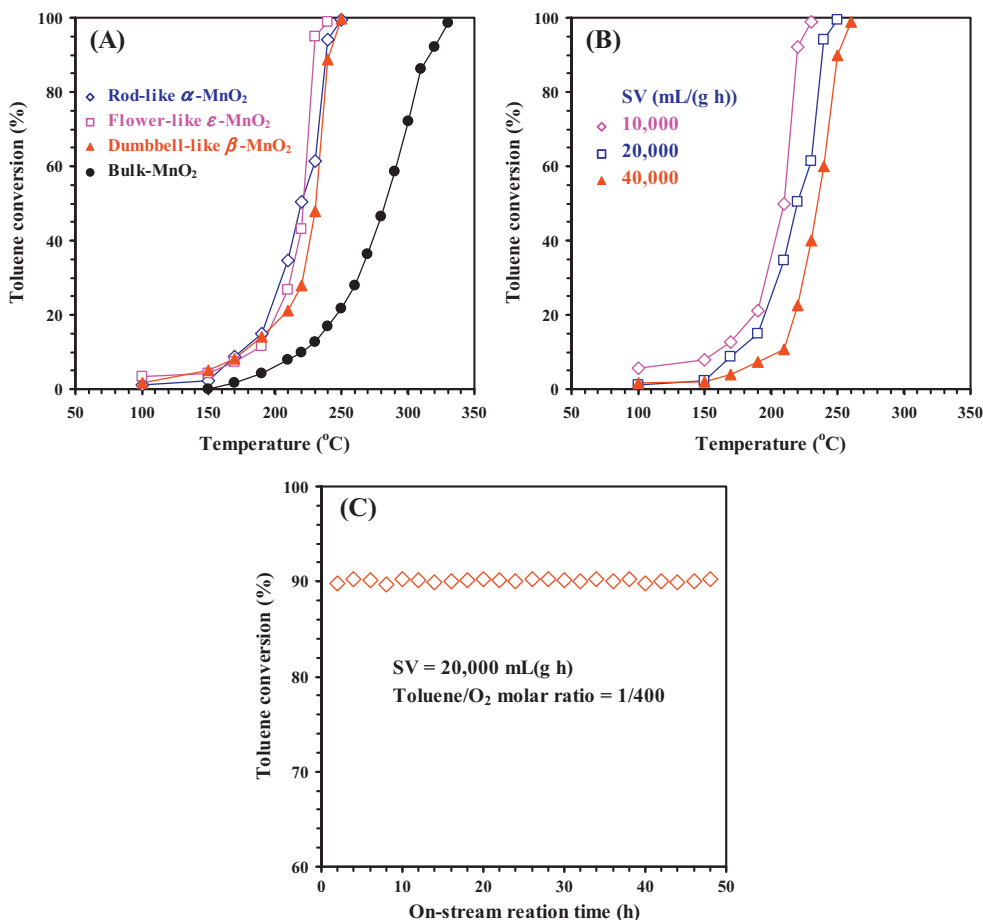


**Fig. 5.** (A) Toluene conversion as a function of reaction temperature over the catalysts under the conditions of toluene concentration = 1000 ppm, toluene/O<sub>2</sub> molar ratio = 1/400, and SV = 20,000 mL/(g h); (B) effect of SV on the catalytic activity of rod-like  $\alpha$ -MnO<sub>2</sub> at toluene/O<sub>2</sub> molar ratio = 1/400; and (C) toluene conversion as a function of on-stream reaction time over the rod-like  $\alpha$ -MnO<sub>2</sub> catalyst at 238 °C.

the lattice oxygen of metal oxides, the latter being re-oxidized by gas-phase oxygen [35–40]. Santos et al. related the lattice oxygen of manganese oxides to reactivity of manganese oxides towards the oxidation of VOCs [37]. Wang et al. suggested that higher reactivity of manganese oxide octahedral molecular sieve catalysts can be assigned to the improvement of oxygen activation, which led to higher reactivity of ethanol and acetaldehyde [38]. In the case of MnO<sub>2</sub>, lattice oxygen of the catalyst can be consumed by reaction with toluene and then be replenished by oxygen from the gas phase [41–43]. Thus, lattice oxygen of manganese oxides can be of great importance in the catalytic oxidation of toluene. The low-temperature reducibility reflects the reactivity of lattice oxygen in MnO<sub>2</sub>. As shown in Fig. 4(A) and (B), the lattice oxygen reactivity decreased in the order of rod-like  $\alpha$ -MnO<sub>2</sub> > flower-like  $\epsilon$ -MnO<sub>2</sub> > dumbbell-like  $\beta$ -MnO<sub>2</sub> > bulk-MnO<sub>2</sub>, in basic agreement with the sequence of the catalytic performance of these samples (flower-like  $\epsilon$ -MnO<sub>2</sub> > rod-like  $\alpha$ -MnO<sub>2</sub> > dumbbell-like  $\beta$ -MnO<sub>2</sub> > bulk-MnO<sub>2</sub>). The formation of surface oxygen vacancies has also an important role to play. These defective sites can be the active centers in the catalytic reaction since oxygen of defective oxides tends to be readily released and transferred, which would enhance the reactivity of the catalyst in oxidation of VOCs [44,45]. It is known that oxygen vacancy, reducibility, and surface area of a transition metal oxide are important factors influencing its catalytic activity [10,13–17]. The presence of oxygen vacancies favors the activation of oxygen molecules to active oxygen adspecies. A good reducibility of the catalyst can provide a facile redox process that would lead

to an enhanced catalytic performance [10,13,46]. The surface area (ca. 132 m<sup>2</sup>/g) of the dumbbell-like  $\beta$ -MnO<sub>2</sub> sample was much higher than those (30–53 m<sup>2</sup>/g) of the rod-like  $\alpha$ -MnO<sub>2</sub> and flower-like  $\epsilon$ -MnO<sub>2</sub> samples, but the catalytic performance of the former was inferior to that of the latter two. This result indicates that surface area was not the key factor governing the catalytic performance. That is to say, other factors should be responsible for the better performance of the rod-like  $\alpha$ -MnO<sub>2</sub> and flower-like  $\epsilon$ -MnO<sub>2</sub> catalysts. As revealed from the XPS and H<sub>2</sub>-TPR studies, the rod-like  $\alpha$ -MnO<sub>2</sub> and flower-like  $\epsilon$ -MnO<sub>2</sub> catalysts possessed higher oxygen adspecies concentrations (relevant to the surface oxygen vacancy densities) and better low-temperature reducibility than the dumbbell-like  $\beta$ -MnO<sub>2</sub> sample, in good agreement with their catalytic activity sequence. Therefore, we conclude that the higher oxygen adspecies concentrations and better low-temperature reducibility mainly accounted for the better catalytic performance of the rod-like  $\alpha$ -MnO<sub>2</sub> and flower-like  $\epsilon$ -MnO<sub>2</sub> samples for toluene combustion.

### 3.5. Kinetic parameters

In the past years, the kinetics of catalytic oxidation of VOCs has been investigated. After studying the oxidation of butyl acetate over the AgZSM-5 catalyst, Wong et al. believed that it was first-order toward butyl acetate concentration and zero toward oxygen concentration [47]. By supposing a first-order kinetics with respect to toluene and a zero-order kinetics with respect to oxygen, Alifanti et al. obtained good linear Arrhenius plots for toluene oxidation

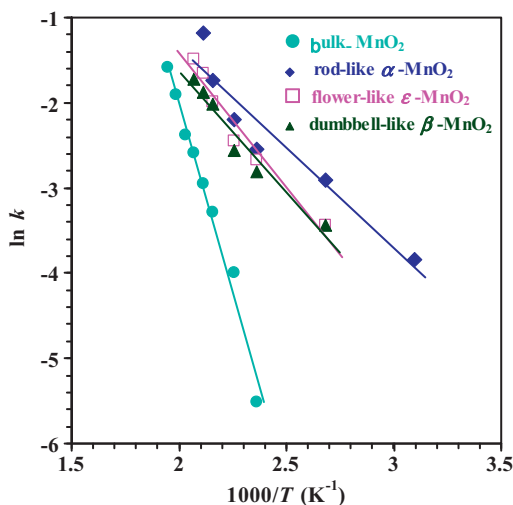


Fig. 6. Arrhenius plots for total oxidation of toluene on the rod-like  $\alpha$ -MnO<sub>2</sub>, flower-like  $\varepsilon$ -MnO<sub>2</sub>, dumbbell-like  $\beta$ -MnO<sub>2</sub>, and bulk-MnO<sub>2</sub> catalysts.

over the ceria-zirconia-supported LaCoO<sub>3</sub> catalyst [48]. Therefore, it is reasonable to assume that the oxidation of toluene in the presence of excess oxygen (toluene/O<sub>2</sub> molar ratio = 1/400) would obey a first-order reaction mechanism with respect to toluene concentration ( $c$ ):

$$r = -kc = -A \exp\left(\frac{-E_a}{RT}\right) c$$

where  $r$  is the reaction rate (mol/s),  $k$  the rate constant (s<sup>-1</sup>),  $A$  the pre-exponential factor, and  $E_a$  the apparent activation energy (kJ/mol). The  $k$  values could be calculated from the reaction rates and reactant conversions at different SV and reaction temperatures.

Fig. 6 shows the Arrhenius plots for the oxidation of toluene at toluene conversion <30% (at which the reaction temperature range was 50–220 °C for the rod-like  $\alpha$ -MnO<sub>2</sub>, flower-like  $\varepsilon$ -MnO<sub>2</sub>, and dumbbell-like  $\beta$ -MnO<sub>2</sub> catalysts and 150–240 °C for the bulk-MnO<sub>2</sub> catalyst). According to the slopes of the Arrhenius plots, one can calculate the rate constants, pre-exponential factors, and apparent activation energies of toluene oxidation over these catalysts, as summarized in Table 2. The  $E_a$  value (74.3 kJ/mol) of the bulk-MnO<sub>2</sub> catalyst was much higher than those (19.6–26.1 kJ/mol) of the  $\alpha$ -,  $\varepsilon$ -, and  $\beta$ -MnO<sub>2</sub> catalysts, with the rod-like  $\alpha$ -MnO<sub>2</sub> catalyst exhibiting the lowest  $E_a$  value (19.6 kJ/mol). The  $E_a$  values obtained over the  $\alpha$ -,  $\varepsilon$ -, and  $\beta$ -MnO<sub>2</sub> catalysts for toluene oxidation were much lower than those (73–89 kJ/mol) over the M<sub>x</sub>Fe<sub>3-x</sub>O<sub>4</sub> (M = Ni, Mn;  $x$  = 0.5–0.65) catalysts [49], those (51–79 kJ/mol) over the 10–20 wt.% LaCoO<sub>3</sub>/Ce<sub>1-x</sub>Zr<sub>x</sub>O<sub>2</sub> ( $x$  = 0–0.2) catalysts [48], and that (62 kJ/mol) over the 7 wt.% Pt/16 wt.% Ce<sub>0.64</sub>Zr<sub>0.15</sub>Bi<sub>0.21</sub>O<sub>1.895</sub>/ $\gamma$ -Al<sub>2</sub>O<sub>3</sub> catalyst [1]. All of the results explain why the  $\alpha$ -,  $\varepsilon$ -, and  $\beta$ -MnO<sub>2</sub> catalysts performed excellently in catalyzing the complete oxidation of toluene at low temperatures.

#### 4. Conclusions

The rod-like tetragonal  $\alpha$ -MnO<sub>2</sub>, flower-like hexagonal  $\varepsilon$ -MnO<sub>2</sub>, and dumbbell-like tetragonal  $\beta$ -MnO<sub>2</sub> catalysts could be prepared using the hydrothermal or water-bathing method. Although the rod-like  $\alpha$ -MnO<sub>2</sub> and flower-like  $\varepsilon$ -MnO<sub>2</sub> samples displayed a lower surface area (30–53 m<sup>2</sup>/g) than the dumbbell-like  $\beta$ -MnO<sub>2</sub> (ca. 132 m<sup>2</sup>/g), the form two samples possessed higher oxygen adspecies concentrations and better low-temperature reducibility than the latter sample. The rod-like  $\alpha$ -MnO<sub>2</sub>, flower-like  $\varepsilon$ -MnO<sub>2</sub>, and dumbbell-like  $\beta$ -MnO<sub>2</sub> catalysts showed much better activities than the bulk-MnO<sub>2</sub> catalyst, with the rod-like

$\alpha$ -MnO<sub>2</sub> and flower-like  $\varepsilon$ -MnO<sub>2</sub> catalyst outperforming the dumbbell-like  $\beta$ -MnO<sub>2</sub> catalyst. Under the conditions of toluene concentration = 1000 ppm, toluene/O<sub>2</sub> molar ratio = 1/400, and SV = 20,000 mL/(g h), the  $T_{90\%}$  value was 238, 229, and 241 °C over rod-like  $\alpha$ -MnO<sub>2</sub>, flower-like  $\varepsilon$ -MnO<sub>2</sub>, and dumbbell-like  $\beta$ -MnO<sub>2</sub>, respectively. The apparent activation energies of the rod-like  $\alpha$ -MnO<sub>2</sub>, flower-like  $\varepsilon$ -MnO<sub>2</sub>, and dumbbell-like  $\beta$ -MnO<sub>2</sub> catalysts were in the range of 20–26 kJ/mol. It is concluded that the higher oxygen adspecies concentrations and better low-temperature reducibility were the main factors responsible for the better catalytic performance of the rod-like  $\alpha$ -MnO<sub>2</sub>, flower-like  $\varepsilon$ -MnO<sub>2</sub>, and dumbbell-like  $\beta$ -MnO<sub>2</sub> materials for the combustion of toluene.

#### Acknowledgments

The work described above was supported by the NSF of Beijing Municipality (Grant No. 2102008), the NSF of China (Grant Nos. 20973017 and 21077007), the National High-Tech Research and Development (863) Program of China (Grant No. 2009AA063201), the Creative Research Foundation of Beijing University Technology (Grant Nos. 00500054R4003 and 005000543111501), and the Funding Project for Academic Human Resources Development in Institutions of Higher Learning under the Jurisdiction of Beijing Municipality (Grant Nos. PHR201007105 and PHR201107104). CTAU thanks the Foundation of the Hong Kong Baptist University (Grant No. FRG2/09-10/023) for financial support. We also thank Mrs. Jianping He (State Key Laboratory of Advanced Metals and Materials, University of Science & Technology Beijing) for doing the SEM analysis.

#### Appendix A. Supplementary data

Supplementary data associated with this article can be found, in the online version, at <http://dx.doi.org/10.1016/j.apcata.2012.05.016>.

#### References

- [1] T. Masui, H. Imadzu, N. Matsuyama, N. Imanaka, J. Hazard. Mater. 176 (2010) 1106–1109.
- [2] V.P. Santos, S.A.C. Carabineiro, P.B. Tavares, M.F.R. Pereira, J.J.M. Órfão, J.L. Figueiredo, Appl. Catal. B 99 (2010) 198–205.
- [3] B. Solsona, T.E. Davies, T. Garcia, I. Vázquez, A. Dejoz, S.H. Taylor, Appl. Catal. B 84 (2008) 176–184.
- [4] C. Lahousse, A. Bernier, E. Gaigneaux, P. Ruiz, P. Grange, B. Delmon, Stud. Surf. Sci. Catal. 110 (1997) 777–785.
- [5] T.K. Tseng, H. Chu, H.H. Hsu, Environ. Sci. Technol. 37 (2003) 171–176.
- [6] H. Rotter, M.V. Landau, M. Herskowitz, Environ. Sci. Technol. 39 (2005) 6845–6850.
- [7] F. Wyrwalski, J.F. Lamonier, S. Siffert, A. Aboukais, Appl. Catal. B 70 (2007) 393–399.
- [8] C. Lahousse, A. Bernier, P. Grange, B. Delmon, P. Papaefthimiou, T. Ioannides, X. Verykios, J. Catal. 178 (1998) 214–222.
- [9] M.A. Peluso, J.E. Sambeth, H.J. Thomas, React. Kinet. Catal. Lett. 80 (2003) 241–248.
- [10] L. Lamaita, M.A. Peluso, J.E. Sambeth, H.J. Thomas, Appl. Catal. B 61 (2005) 114–119.
- [11] L. Lamaita, M.A. Peluso, J.E. Sambeth, H.J. Thomas, G. Minelli, P. Porta, Catal. Today 107/108 (2005) 133–138.
- [12] M.A. Peluso, E. Proncato, J.E. Sambeth, H.J. Thomas, G. Busca, Appl. Catal. B 78 (2008) 73–79.
- [13] J.Q. Torres, J.-M. Giraudon, J.-F. Lamonier, Catal. Today 176 (2011) 277–280.
- [14] V.P. Santos, M.F.R. Pereira, J.J.M. Órfão, J.L. Figueiredo, Top. Catal. 52 (2009) 470–481.
- [15] L. Zhou, J.H. He, J. Zhang, Z.C. He, Y.C. Hu, C.B. Zhang, H. He, J. Phys. Chem. C 115 (2011) 16873–16878.
- [16] L. Zhou, J. Zhang, J.H. He, Y.C. Hu, H. Tian, Mater. Res. Bull. 46 (2011) 1714–1722.
- [17] S.C. Kim, W.G. Shim, Appl. Catal. B 98 (2010) 180–185.
- [18] Y.S. Xia, H.X. Dai, L. Zhang, J.G. Deng, H. He, C.T. Au, Appl. Catal. B 100 (2010) 229–237.
- [19] Y.S. Xia, H.X. Dai, H.Y. Jiang, J.G. Deng, H. He, C.T. Au, Environ. Sci. Technol. 43 (2009) 8355–8360.

- [20] Y.S. Xia, H.X. Dai, H.Y. Jiang, L. Zhang, J.G. Deng, C.T. Au, *J. Hazard. Mater.* 186 (2011) 84–91.
- [21] J.G. Deng, L. Zhang, H.X. Dai, Y.S. Xia, H.Y. Jiang, H. Zhang, H. He, *J. Phys. Chem. C* 114 (2010) 2694–2700.
- [22] Y.S. Xia, H.X. Dai, H.Y. Jiang, L. Zhang, *Catal. Commun.* 11 (2010) 1171–1175.
- [23] S.H. Liang, F. Teng, G. Bulgan, R.L. Zong, Y.F. Zhu, *J. Phys. Chem. C* 112 (2008) 5307–5315.
- [24] B.X. Li, G.X. Rong, Y. Xie, L.F. Huang, C.Q. Feng, *Inorg. Chem.* 45 (2006) 6404–6410.
- [25] W. Xiao, D.L. Wang, X.W. Lou, *J. Phys. Chem. C* 114 (2010) 1694–1700.
- [26] J.F. Moulder, W.F. Stickle, P.E. Sobol, K.D. Bomben, *Handbook of X-ray photoelectron spectroscopy*, in: J. Chastain, R.C. King Jr. (Eds.), *Physical Electronics*, Eden Prairie, 1995, p. 78.
- [27] J.C. Carver, G.K. Schweitzer, *J. Chem. Phys.* 57 (1972) 973–982.
- [28] S. Ponce, M.A. Peña, J.L.G. Fierro, *Appl. Catal. B* 24 (2000) 193–205.
- [29] S.D. Gardner, G.B. Hoflund, M.R. Davidson, D.R. Schryer, J. Schryer, B.T. Upchurch, E.J. Kielin, *Langmuir* 7 (1991) 2135–2139.
- [30] K.D. Chen, S.B. Xie, A.T. Bell, E. Iglesia, *J. Catal.* 198 (2001) 232–242.
- [31] H.X. Dai, A.T. Bell, E. Iglesia, *J. Catal.* 221 (2004) 491–499.
- [32] M.P. Irusta, M. Pina, J. Menéndez, Santamaría, *J. Catal.* 179 (1998) 400–412.
- [33] S. Scirè, S. Minicò, C. Crisafulli, C. Satriano, A. Pistone, *Appl. Catal. B* 40 (2003) 43–49.
- [34] A. Musialik-Piotrowska, H. Landmesser, *Catal. Today* 137 (2008) 357–361.
- [35] Y.F. Chang, J.G. McCarty, *Catal. Today* 30 (1996) 163–170.
- [36] B. Grbic, N. Radic, B. Markovic, P. Stefanov, D. Stoychev, Ts Marinova, *Appl. Catal. B* 64 (2006) 51–56.
- [37] V.P. Santos, M.F.R. Pereira, J.J.M. Órfão, J.L. Figueiredo, *Appl. Catal. B* 99 (2010) 353–363.
- [38] R.H. Wang, J.H. Li, *Environ. Sci. Technol.* 44 (2010) 4282–4287.
- [39] V. Roche, L. Mazri, A. Boréave, M.H. Ta, L. Retailleau-Mevel, A. Giroir-Fendler, P. Vernoux, J.P. Deloume, *Appl. Catal. A* 385 (2010) 163–169.
- [40] Y.S. Wu, Y.X. Zhang, M. Liu, Z.C. Ma, *Catal. Today* 153 (2010) 170–175.
- [41] M. Baldi, E. Finocchio, F. Milella, G. Busca, *Appl. Catal. B* 16 (1998) 43–51.
- [42] C. Cellier, V. Ruaux, C. Lahousse, P. Grange, E.M. Gaigneaux, *Catal. Today* 117 (2006) 350–355.
- [43] J. Luo, Q. Zhang, J. Garcia-Martinez, S.L. Suib, *J. Am. Chem. Soc.* 130 (2008) 3198–3207.
- [44] X. Chen, Y.F. Shen, S.L. Suib, C.L. O'Young, *J. Catal.* 197 (2001) 292–302.
- [45] Q.H. Tang, T. Liu, Y.H. Yang, *Catal. Commun.* 9 (2008) 2570–2573.
- [46] A.R. Gandhe, J.S. Rebelló, J.L. Figueiredo, J.B. Fernandes, *Appl. Catal. B* 72 (2007) 129–135.
- [47] C.T. Wong, A.Z. Abdullah, S. Bhatia, *J. Hazard. Mater.* 157 (2008) 480–489.
- [48] M. Alifanti, M. Florea, S. Somacescu, V.I. Pârvulescu, *Appl. Catal. B* 60 (2005) 33–39.
- [49] M. Florea, M. Alifanti, V.I. Pârvulescu, D. Mihaila-Tarabasanu, L. Diamandescu, M. Feder, C. Negrila, L. Frunza, *Catal. Today* 141 (2009) 361–366.